

Resonant Spin-Flavor Conversion of Supernova Neutrinos and Deformation of the Electron Antineutrino Spectrum

Tomonori Totani¹ and Katsuhiko Sato^{1,2}

¹*Department of Physics, School of Science, The University of Tokyo,
7-3-1 Hongo, Tokyo 113, Japan.*

e-mail: totani@utaph1.phys.s.u-tokyo.ac.jp

²*Research Center for the Early Universe, School of Science, The University of Tokyo,
7-3-1 Hongo, Tokyo 113, Japan.*

Abstract

The neutrino spin-flavor conversion of $\bar{\nu}_e \leftrightarrow \nu_\mu$ which is induced by the interaction of the neutrino magnetic moment and magnetic fields in the collapse-driven supernova is investigated in detail. We calculate the conversion probability by using the latest precollapse models of Woosley and Weaver (1995), and also those of Nomono and Hashimoto (1988), changing the stellar mass and metallicity in order to estimate the effect of the astrophysical uncertainties. Contour maps of the conversion probability are given for all the models as a function of neutrino mass squared difference over neutrino energy ($\Delta m^2/E_\nu$) and the neutrino magnetic moment times magnetic fields ($\mu_\nu B$). The expected deformation of the $\bar{\nu}_e$ spectrum can be clearly seen from these maps, and some qualitative features which will be useful in the future observation are summarized. It is shown that in the solar metallicity models some observational effects are expected with $\Delta m^2 = 10^{-5}$ – 10^{-1} [eV²] and $\mu_\nu \gtrsim 10^{-12} (10^9 \text{G}/B_0) [\mu_B]$, where B_0 is the strength of the magnetic fields at the surface of the iron core, and $B_0 = 10^9$ [Gauss] is a reasonable value which is inferred from the observed magnetic fields in white dwarfs. We also find that although the dependence on the stellar models or stellar mass is not so large, the metallicity of precollapse stars has considerable effects on this conversion. In lower metallicity stars, strong precession between $\bar{\nu}_e$ and ν_μ occurs with small $\Delta m^2/E_\nu$ ($\lesssim 10^{-8}$ [eV²/MeV]), and conversion probability changes periodically with B_0 . Such effects may be seen in a supernova in the Large or Small Magellanic Clouds, and should be taken into account when one considers an upper bound on μ_ν from the SN1987A data.

I. INTRODUCTION

Copious neutrino emission from collapse-driven supernovae attracts significant attention because it provides rich information not only on the mechanism of supernovae but also on the neutrino physics through a number of events captured in some underground neutrino detectors, such as the Super-Kamiokande (SK) [1]. The most noteworthy subject on the nature of neutrinos is the mass of neutrinos and oscillations between different flavors induced by the mass difference. However, the ordinary matter oscillation (well known as the MSW effect [2]) has its effect only on neutrinos but not on antineutrinos under the direct mass hierarchy, and the vacuum oscillation is not observable unless the mixing angle is unnaturally large compared with that of the quark sector. In this case, electron antineutrinos ($\bar{\nu}_e$'s), which is the most detectable in a water Čerenkov detector, do not undergo any oscillation. One of some possibilities that $\bar{\nu}_e$'s would oscillate or be converted into other species of neutrinos is the neutrino magnetic moment. If the neutrinos have a nonvanishing magnetic moment, it couples the left- and right-handed neutrinos, and interaction with sufficiently strong magnetic fields induces the precession between neutrinos with different chiralities in the inner region of the collapse-driven supernova [3,4]. In general, non-diagonal elements of the magnetic moment matrix are possible, and neutrinos can be changed into different flavors by this flavor changing moment [5]. Furthermore, with the additional effect of the coherent forward scattering by dense matter in the collapsing star, neutrinos can be resonantly converted¹ into neutrinos with different chiralities [6–11] by the mechanism similar to the MSW effect. This resonant spin-flavor conversion induced by the neutrino magnetic moment may drastically deform the spectrum of electron antineutrinos ($\bar{\nu}_e$'s) in the water Čerenkov detectors. The earlier publications have shown that in the future experiment this effect will be observable with inner magnetic fields of some reasonable strength, if there is a magnetic moment a little smaller than the current astrophysical upper limits from the argument of the stellar cooling due to the plasmon decay²: $\mu_\nu \lesssim 10^{-11}\text{--}10^{-10}\mu_B$, where μ_B is the Bohr magneton [12,13]. The magnetic moment of neutrinos in the standard electro-weak theory with small neutrino masses is very small due to the chirality suppression; for example, the standard $SU(2)_L \times U(1)$ model with a singlet right-handed neutrino gives $\mu_\nu \sim 3 \times 10^{-19}(m_\nu/1\text{eV})\mu_B$, far below the experimental/astrophysical upper bounds [4,14–16]. However, some particle-physics models [17,18] have been proposed in order to give a large magnetic moment of $\sim 10^{-11}\mu_B$ which would explain [19–21] the anticorrelation between the time variability of the solar neutrino flux and the sun spot numbers suggested in the ^{37}Cl experiment [22]. (The anticorrelation in the Cl experiment, however, has not yet been statistically settled.) Therefore, the influence of a large magnetic moment on various physical or astrophysical phenomena including collapse-driven supernovae deserves more detailed investigation. Discovery of a large magnetic moment of neutrinos indicates that there exist interactions which violate the chirality conservation beyond the standard theory.

In this paper, the resonant spin-flavor conversion between right-handed $\bar{\nu}_e$'s and left-handed

¹The precession itself is suppressed by the matter potential.

²This constraint refers to the norm of the neutrino magnetic moment matrix, $(\sum_{i,j} |\mu_{ij}|^2)^{1/2}$, i.e., this includes the flavor changing moment.

mu or tau neutrinos (ν_μ or ν_τ 's) is studied assuming that the neutrino is the Majorana particle. In general, the matter potential suppresses the interaction of the magnetic moment and magnetic fields because of the generated difference of the energy levels. However, Athar et al. [11] pointed out that the resonant conversion of this mode ($\bar{\nu}_e \leftrightarrow \nu_\mu$) occurs quite effectively in the region above the iron core and below the hydrogen envelope of collapsing stars, namely, in the O+Si, O+Ne+Mg, O+C, and He layers (hereafter referred to ‘the isotopically neutral region’). The reason is that the effective matter potential for the $\bar{\nu}_e \leftrightarrow \nu_\mu$ mode is given in the form proportional to the value of $(1 - 2Y_e)$, where Y_e is the electron number fraction per nucleon, and Y_e is very close to 0.5 in this region (typically, $(1 - 2Y_e) \sim 10^{-4}$ – 10^{-3}); the matter effect is therefore strongly suppressed compared with the magnetic interaction, and the adiabaticity condition becomes considerably less stringent. Athar et al. [11] have shown that assuming $\mu_\nu (= \mu_{\bar{\nu}_e \nu_\mu}) \sim 10^{-12} \mu_B$, this resonant conversion would occur with some reasonable assumptions about magnetic fields in a star. We also consider μ_ν around this value³.

In order to judge the deformation of an observed $\bar{\nu}_e$ spectrum as the evidence of the existence of the neutrino magnetic moment, it is necessary that the conversion probability is calculated with high accuracy in a wide range of some parameters such as the mass of neutrinos or the magnetic fields. However, only rough estimates or demonstrations in some cases are given in the earlier publications and the relation between the shape of the deformed spectrum and the physical parameters has not yet been clarified. Therefore we make the contour maps of the conversion probability of $\bar{\nu}_e \leftrightarrow \nu_\mu$ for some used models of precollapse stars as a function of the two parameters: $\Delta m^2/E_\nu$ and $\mu_\nu B_0$, where Δm^2 is the neutrino mass squared difference, E_ν the neutrino energy, and B_0 the magnetic field at the surface of the iron core. The expected observational effects can be clearly understood by these maps. Some examples of spectral deformation are also calculated and qualitative features which will be useful for the future observation are summarized by using these maps.

It is apparent that the deviation of the value of Y_e from 0.5 in the isotopically neutral region is quite important, and this value is strongly dependent on the isotopic composition. Since almost all nuclei in the isotopically neutral region are symmetric in the number of neutrons and protons, this deviation is determined by rarely existent nuclei and the accurate estimate of this deviation is quite difficult. Therefore, the astrophysical uncertainty in $(1 - 2Y_e)$ should be discussed. We use the latest 15 and 25 M_\odot precollapse models of Woosley and Weaver (hereafter WW) [25] which include no less than 200 isotopes. Such a large number of isotopes have never been used previously in the calculation of $(1 - 2Y_e)$. It is also expected that this value strongly depends on the stellar metallicity, and hence we use the WW models with the two different metallicities: the solar and zero metallicity, and the metallicity effect is investigated. Also the models of 4 and 8 M_\odot helium core of Nomoto & Hashimoto [26] (hereafter NH) are used, which correspond approximately to 15 and 25 M_\odot main sequence stars, and the model dependence of $(1 - 2Y_e)$ is discussed.

³There is a further stringent constraint on the transition magnetic moment of massive neutrinos from observation of the 21-cm (hyperfine) radiation from neutral hydrogen gas in external galaxies: $\mu_\nu \leq 1.7 \times 10^{-15}$ for the neutrino masses above 30 eV [23,24]. However, we consider only the range of $\Delta m^2 \lesssim 1$ [eV²] and this upper bound does not constrain our analysis.

We consider Δm^2 smaller than about 1 [eV²], therefore the resonance occurs above the surface of the iron core. The resonance in the iron core and its implications on the dynamics of the supernova considered in a recent preprint [27] are not discussed here. The global structure of magnetic field is assumed to be a dipole moment, and the strength of the magnetic field is normalized at the surface of the iron core with the values of 10^8 – 10^{10} [Gauss], which are inferred from the observation of the magnetic fields on the surface of white dwarfs. Throughout this paper, we consider the conversion between two generations for simplicity. Because ν_μ and ν_τ can be regarded as identical particles in the collapse-driven supernova, our results also apply to the conversion of $\bar{\nu}_e \leftrightarrow \nu_\tau$. Derivation of the equation which describes the propagation of neutrinos and evolution of conversion probability is given in section II, and the profile of the effective matter potential and magnetic fields are given in section III by using the precollapse models of massive stars. Qualitative features of the conversion are also discussed in this section. Numerical results are given in section IV, and spectral deformation is also discussed. Discussion and conclusions are given in sections V and VI, respectively.

II. FORMULATIONS

The interaction of the magnetic moment of neutrinos and magnetic fields is described as

$$\langle (\nu_i)_R | H_{\text{int}} | (\nu_j)_L \rangle = \mu_{ij} B_\perp , \quad (1)$$

where μ_{ij} is the magnetic moment matrix, B_\perp the magnetic field transverse to the direction of propagation, $(\nu)_R$ and $(\nu)_L$ the right- and left-handed neutrinos, respectively, and i and j denote the flavor eigenstate of neutrinos, i.e., e , μ , and τ . The magnetic moment interacts only with transverse magnetic fields. If neutrinos are the Dirac particles, right-handed neutrinos and left-handed antineutrinos do not interact with matter and therefore undetectable. The conversion into these sterile neutrinos due to the magnetic moment suffers strong constraints from the observation of neutrinos from SN1987A by the Kamiokande II [28] and IMB [29], and also from the argument on energy transportation in the collapse-driven supernova [8,10,30–33]. On the other hand, if neutrinos are the Majorana particles, as assumed in this paper, ν_R 's are antineutrinos and interact with matter, and the constraint becomes considerably weak. The diagonal magnetic moment is forbidden for the Majorana neutrinos, and therefore only the conversion between different flavors is possible, e.g., $(\bar{\nu}_e)_R \leftrightarrow (\nu_{\mu,\tau})_L$. As mentioned in introduction, we investigate this mode because the conversion of this mode occurs quite effectively in the isotopically neutral region and also $\bar{\nu}_e$'s are most easily detected in the water Čerenkov detectors.

In dense matter of the collapsing stars, the coherent forward scattering by matter leads to the effective potential for neutrinos, and this potential for each type of neutrinos is determined according to the weak interaction theory. The potential due to scattering with electrons is given as (including both the charged- and neutral-current interactions)

$$V = \pm \sqrt{2} G_F \left(\pm \frac{1}{2} + 2 \sin^2 \theta_W \right) n_e , \quad (2)$$

where n_e is the number density of electrons, G_F the Fermi coupling constant, and θ_W the Weinberg angle. The \pm sign in the parentheses refers to ν_e (+) and $\nu_{\mu,\tau}$ (–), and that in front to ν (+)

and $\bar{\nu}$ ($-$). In the ordinary flavor oscillation ($\nu_e \leftrightarrow \nu_{\mu,\tau}$), the effective potential is only due to the charged-current scattering by electrons because the effect of neutral-current interactions is the same for all flavors. However, we have to consider the neutral-current interaction in the conversion of ν and $\bar{\nu}$, because of the opposite signs of the potential. Therefore the neutral-current scattering by nucleons should also be included, that is

$$V = \pm\sqrt{2} G_F \left(\frac{1}{2} - 2\sin^2\theta_W\right) n_p \mp \sqrt{2} G_F \frac{1}{2} n_n, \quad (3)$$

where n_p is the number density of protons, n_n that of neutrons. The \pm or \mp signs refer to ν (upper) and $\bar{\nu}$ (lower) for all three flavors of neutrinos. We do not have to consider the form factor of nuclei because the relevant interaction is forward scattering and there is no momentum transfer. The isotopically neutral region is far beyond the neutrino sphere and neutrinos go out freely in this region; hence we do not have to consider the neutrino-neutrino scattering. By using the charge neutrality, the difference of the potentials for $\bar{\nu}_e$'s and ν_μ 's (or ν_τ 's) which we are interested in is as follows:

$$\Delta V \equiv V_{\bar{\nu}_e} - V_{\nu_\mu} = \sqrt{2}G_F\rho/m_N(1 - 2Y_e), \quad (4)$$

where ρ is the density, m_N the mass of nucleons, and $Y_e = n_p/(n_p + n_n)$. Now the time evolution of the mixed state of $\bar{\nu}_e$ and ν_μ is described by the following Schrödinger equation:

$$i\frac{d}{dr} \begin{pmatrix} \bar{\nu}_e \\ \nu_\mu \end{pmatrix} = \begin{pmatrix} 0 & \mu_\nu B_\perp \\ \mu_\nu B_\perp & \Delta H \end{pmatrix} \begin{pmatrix} \bar{\nu}_e \\ \nu_\mu \end{pmatrix}, \quad (5)$$

and ΔH is defined as:

$$\Delta H \equiv \frac{\Delta m^2}{2E_\nu} \cos 2\theta - \Delta V, \quad (6)$$

where E_ν is the energy of neutrinos, $\Delta m^2 = m_2^2 - m_1^2$, θ the angle of the vacuum generation mixing, and r the radius from the center of the star. Here we consider only $\bar{\nu}_e$ and ν_μ , but this equation is actually a truncation of the original 4-component (ν_e , ν_μ , and antineutrinos) equation (see ref. [6]). The neutrino masses, m_1 and m_2 are those in the mass eigenstates ($m_2 > m_1$). The direct mass hierarchy is assumed here and therefore Δm^2 is positive. The other terms have their standard meanings and the units of $c = \hbar = 1$ are used. Also note that we can subtract an arbitrary constant times the unit matrix from the Hamiltonian, which does not affect the probability amplitudes. In the MSW flavor oscillation, there appears the term of generation mixing, $\Delta m^2 \sin 2\theta/4E_\nu$, in the off-diagonal elements of the Hamiltonian; however, this term does not appear in this spin-flavor conversion between neutrinos and antineutrinos. In the following, μ_ν and $\cos 2\theta$ are set to be $10^{-12}\mu_B$ and 1, respectively, and the scaling of B or Δm^2 with respect to other values of μ_ν or $\cos 2\theta$ is obvious. The resonant spin-flavor conversion occurs when the difference of the diagonal elements in the Hamiltonian vanishes, and hence the resonance condition is given as $\Delta H = 0$. By using this equation, the probability of conversion can be calculated provided that $\rho(r)$, $Y_e(r)$, and $B_\perp(r)$ are known.

III. ASTROPHYSICAL ASPECTS

A. Effective Matter Potential

In this section, we consider the effective matter potential in the isotopically neutral region. The value of $(1 - 2Y_e)$ which we are interested in is easily calculated as:

$$Y_e - \frac{1}{2} = \sum_i \left(\frac{Z_i}{A_i} - \frac{1}{2} \right) X_i, \quad (7)$$

where Z_i , A_i , and X_i are the atomic number, mass number, and the mass fraction of the i -th isotope, respectively, and the subscript i runs over all isotopes with $2Z \neq A$. In order to get this value and the density profiles, the precollapse models of massive stars of Woosley & Weaver (WW) [25] and Nomoto & Hashimoto (NH) [26] are used. We assume that the dynamical effect can be ignored within the time scale of the neutrino emission, and hence use the above static models. The mass and radius of the helium core of a $15M_\odot$ main sequence star is $\sim 4M_\odot$ and $\sim 1R_\odot$, respectively, and its free-fall time scale, $(\sqrt{G\rho})^{-1}$ is $\sim 10^2$ – 10^3 [sec], which is longer than the neutrino emission time scale (at most a few tens of seconds). It takes about several tens of seconds for the shock wave generated at the core bounce to reach the hydrogen envelope [25], and the inner region of the isotopically neutral region may be disturbed by the shock wave. We will discuss about this in section V. The calculation of the WW models of 15 and 25 M_\odot (hereafter WW15 and WW25, respectively) includes 200 isotopes, up to ^{71}Ge . Although the network of 19 isotopes is used for energy generation up to the end of oxygen burning, the network of 200 isotopes is updated in each cycle and mixed using the same diffusion coefficients. The NH models are 4 and 8 M_\odot helium cores (hereafter NH4 and NH8, respectively) corresponding approximately to 15 and 25 M_\odot main sequence stars. Their calculation includes 30 isotopes up to the end of oxygen burning, which are also used for the energy generation. The WW and NH models use the different reaction rates of $^{12}\text{C}(\alpha, \gamma)^{16}\text{O}$, and the treatment of convection is also different. As for the WW models, we use the models with two different metallicities: the solar and zero metallicity, and the metal abundance of the NH models is that of the Sun.

By using the data of composition as well as the density profile of the solar metallicity WW models (WW15S and WW25S, where ‘S’ denotes the solar metallicity), $|\Delta V|$ in the WW15S and WW25S models are depicted in Figs. 1 and 2, respectively, by the thick solid lines as a function of the radius from the center of the star. Also shown by the dashed lines is $|\Delta H|$ when $\Delta m^2/E_\nu$ is 10^{-4} and 10^{-6} [eV²/MeV]. The dominantly existent nuclei are also indicated for each layer in the top of these figures. In the neutronized iron core, Y_e is smaller than 0.5, and ΔV is positive and much larger than $\Delta m^2/E_\nu$ unless $\Delta m^2/E_\nu$ is larger than 10^{-1} [eV²/MeV]. We consider the range of $\Delta m^2/E_\nu$ below this value, and hence the resonance does not occur in the iron core. Above the iron core, i.e., in the isotopically neutral region, Y_e becomes quite close to 0.5 (still $Y_e < 0.5$) and ΔV is strongly suppressed, typically by a factor of $\sim 10^{-3}$ in solar metallicity stars, and the term $\mu_\nu B$ becomes more effective. This suppression continues to the end of the isotopically neutral region, namely, just below the hydrogen envelope. The isotopically neutral region is roughly divided into the four layers: O+Si, O+Ne+Mg, O+C, and He layer, from inner to outer region. The values of $(1 - 2Y_e)$ and some nuclei which are relevant to the deviation of Y_e from 0.5 are tabulated in Table

I for each layer and for the six precollapse models used in this paper. For the solar metallicity models, $(1 - 2Y_e)$ is determined mainly by the isotopes such as ^{22}Ne , $^{25,26}\text{Mg}$, ^{27}Al , ^{34}S , ^{38}Ar , and so on.

The resonance occurs when ΔV becomes smaller than $\Delta m^2/2E_\nu$, and after the resonance (above the resonance layer) ΔH becomes constant with radius because ΔV is negligibly small. If the strength of the magnetic field is sufficiently strong for the satisfaction of the adiabaticity condition at the resonance layer, the neutrinos are resonantly converted into the other helicity state. The magnetic fields and the adiabaticity condition are discussed in the following subsection. The resonance layer is in the isotopically neutral region if $\Delta m^2/E_\nu$ is in the range of roughly 10^{-10} – 10^{-1} [eV^2/MeV] (slightly dependent on the stellar models), and the resonance layer moves inward with increasing $\Delta m^2/E_\nu$. If $\Delta m^2/E_\nu$ is smaller than 10^{-10} [eV^2/MeV], the mass term has no effect on ΔH in this region of the solar metallicity models, and the resonance occurs at the boundary between the helium layer and the hydrogen envelope due to the change of the sign of $(1 - 2Y_e)$. In contrast with the flavor oscillation, the matter potential changes its sign by itself and the resonance can occur without the mass term, $\Delta m^2/E_\nu$. However, as explained in the next subsection, if a dipole moment is assumed as the global structure of the magnetic fields, it seems difficult that B is strong enough to satisfy the adiabaticity condition at this boundary in the solar metallicity models. In the hydrogen envelope, Y_e is about 0.8 and the suppression of $(1 - 2Y_e)$ does not work any more. We can see that most of the qualitative features are the same for the two models: WW15S and WW25S, and the dependence on the stellar masses is rather small. Note that our result gives 1–2 orders of magnitude larger ΔV than that in the earlier calculation by Athar et al. [11], in which the older $15 M_\odot$ Woosley & Weaver model [34,35] is used. It is probably because our calculation of $(1 - 2Y_e)$ includes the larger network of isotopes used in the latest WW models.

In Figs. 3 and 4, we show the same with Figs. 1 and 2, but for the Nomoto & Hashimoto models. It can be seen that the profiles of ΔV of the WW and NH models are not so different, and the model dependence seems rather small. However, the situation is drastically changed when we consider the effect of different metallicities. Figs. 5 and 6 are the same with Figs. 1 and 2, but for the zero metallicity WW models: WW15Z and WW25Z. ('Z' denotes the zero metallicity.) In the O+Si and O+Ne+Mg layers, $(1 - 2Y_e)$ is smaller than that of the solar metallicity models by about 1 order of magnitude, and in the O+C and He layers, $(1 - 2Y_e)$ is further strongly suppressed (4–6 orders of magnitudes) because of the lack of the heavy nuclei which cause the deviation of Y_e from 0.5 (Table I). In consequence, the metallicity effect becomes especially important when $\Delta m^2/E_\nu$ is smaller than $\sim 10^{-6}$ [eV^2/MeV]. How this effect changes the profile of the conversion probability will be discussed in more detail in section IV.

B. Magnetic Fields

Let us consider the magnetic fields in the isotopically neutral region. In the earlier publication [11], the strength of magnetic fields was normalized at the surface of the newly born neutron star ($r \sim 10$ km), but it is unlikely that the magnetic fields of a nascent neutron star have some effects on the far outer region, such as the isotopically neutral region, within the short time scale of the neutrino burst. The magnetic fields should be normalized by the fields which are static and existent before the core collapse. The strength of such magnetic fields above the surface of the iron

core may be inferred from that observed on the surface of white dwarfs, because the iron core of giant stars is similar to white dwarfs in the point that both are sustained against the gravitational collapse by the degenerate pressure of electrons. The observations of the magnetic fields in white dwarfs show that the strength spreads in a wide range of 10^7 – 10^9 Gauss [36]. Taking account of the possibility of the decay of magnetic fields in white dwarfs, it is not unnatural to consider the magnetic fields up to 10^{10} Gauss at the surface of the iron core. As for the global structure of the fields, although the optimistic estimate of $B \propto r^{-2}$ is sometimes discussed from the argument of the flux freezing, a magnetic dipole is natural as static and global fields; we hence assume such fields in this paper. Therefore the off-diagonal element of the Hamiltonian in Eq.(5), $\mu_\nu B_\perp$ becomes $\mu_\nu B_0 (r_0/r)^3 \sin \Theta$, where B_0 is the strength of the magnetic field at the equator on the iron core surface, r_0 the radius of the iron core, and Θ the angle between the pole of the magnetic dipole and the direction of neutrino propagation. If the magnetic field is normalized at the surface of the neutron star, the radial dependence of a dipole ($\propto r^{-3}$) gives too small field in the isotopically neutral region, but the normalization at the surface of the iron core inferred from the observations of white dwarfs makes it possible that the magnetic field is sufficiently strong in the isotopically neutral region under the condition of a global dipole moment. The lines of $\mu_\nu B$ [eV] are shown in Figs. 1–6 for $B_0 = 10^8$ and 10^{10} [Gauss], assuming $\mu_\nu = 10^{-12} \mu_B$. The strength of magnetic fields is also discussed from the argument of energetics. The energy density of the maximum strength of magnetic fields should at most be the same order of magnitudes with that of the thermal plasma in the star. Let us define the magnetic fields B_{th} , whose energy density is the same with that of the gas in the star:

$$\frac{1}{8\pi} B_{th}^2 = \frac{3}{2} \frac{\rho}{\tilde{\mu} m_p} kT, \quad (8)$$

where ρ is the density, T temperature, k the Boltzmann constant, and $\tilde{\mu}$ the mean molecular weight. The line of $\mu_\nu B_{th}$ is depicted in Figures 1–6, assuming $\tilde{\mu} = 1$ and $\mu_\nu = 10^{-12} \mu_B$, and it can be seen that the magnetic fields up to $B_0 \sim 10^{10}$ [Gauss] are far below B_{th} and therefore natural from the view point of energetics.

If there is no matter potential, the complete precession of $\nu_R \leftrightarrow \nu_L$ occurs; however, the precession amplitude is suppressed by the matter potential. The precession amplitude is given in the form [11,19]:

$$A_p = \frac{(2\mu_\nu B)^2}{(2\mu_\nu B)^2 + (\Delta H)^2}. \quad (9)$$

In the neutronized iron core, ΔH is much larger than $\mu_\nu B$ even when $B_0 \sim 10^{10}$ [Gauss], and the precession below the surface of the iron core can be completely neglected. (In other words, we can start the calculation with the pure neutrino states from the iron core surface, with $B_0 \lesssim 10^{10}$ [Gauss].) Above the iron core, i.e., in the isotopically neutral region in the solar metallicity models, $\mu_\nu B$ is still much lower than ΔV (or ΔH), except at the resonance layer or the boundary of the helium layer and the hydrogen envelope, as shown in Figs. 1–4. Therefore, the precession does not occur in the solar metallicity stars. However, if the strength of the magnetic fields is strong enough to satisfy the adiabaticity condition at the resonance layer, neutrinos are resonantly converted into other types of neutrinos. The adiabaticity condition is satisfied when the precession length at the resonance layer, $(\mu_\nu B)^{-1}$, is shorter than the thickness of the resonance layer, i.e.,

$$\mu_\nu B \gtrsim \left| \frac{d(\Delta H)}{dr} \right|^{\frac{1}{2}} = \left| \frac{d(\Delta V)}{dr} \right|^{\frac{1}{2}} \quad (\text{at the resonance}), \quad (10)$$

since the thickness of the resonance layer, Δr_{res} , is given as

$$\Delta r_{\text{res}} = \mu_\nu B \left(\left| \frac{d(\Delta H)}{dr} \right| \right)^{-1}. \quad (11)$$

Note that the suppression of $(1 - 2Y_e)$ in the isotopically neutral region makes the adiabaticity condition well satisfied because it reduces the right hand side of Eq.(10) by a factor of $(1 - 2Y_e)^{1/2}$. In order to show how this condition is satisfied, $|d(\Delta V)/dr|^{1/2}$ is shown by the thin solid lines in Figs. 1–6. If $\mu_\nu B$ is (roughly) larger than $|d(\Delta V)/dr|^{1/2}$ at the resonance layer ($\Delta H = 0$), the adiabaticity condition is satisfied and $\bar{\nu}_e$'s and ν_μ 's are mutually converted. In both the WW and NH models with the solar metallicity, the region where this condition is satisfied appears with $B_0 \gtrsim 10^{10}$ [Gauss]. Because the slope of $|d(\Delta V)/dr|^{1/2}$ is flatter than that of $\mu_\nu B$, this condition is satisfied better in the inner region of the star, in other words, with large values of $\Delta m^2/E_\nu$, in the solar metallicity models. When $\Delta m^2/E_\nu$ is smaller than $\sim 10^{-10}$ [eV²/MeV] and the resonance layer lies at the boundary of the helium layer and the hydrogen envelope, unnaturally strong magnetic fields are necessary for satisfaction of the adiabaticity condition. However, in the zero metallicity stars, because the value of $(1 - 2Y_e)$ is very strongly suppressed in the O+C and He layers, $\mu_\nu B$ becomes much larger than ΔH and hence the strong precession between different chiralities occurs with small $\Delta m^2/E_\nu$ (Figs. 5 and 6). Since the adiabaticity may be broken at the quite large jump of the matter potential at the boundary of the helium layer and the hydrogen envelope, the detailed calculation is necessary for the conversion probability when $\Delta m^2/E_\nu \lesssim 10^{-8}$ [eV²/MeV]. It is apparent that the conversion probability in zero metallicity stars will be completely different from the solar metallicity stars. Now all of the qualitative features of the conversion can be understood from Figs. 1–6 and the results of final conversion probability obtained by solving the evolution equation (Eq. 5) numerically are given in the following section.

IV. RESULTS

A. Conversion Probability Maps

In this section the contour maps of the conversion probability ($\bar{\nu}_e \leftrightarrow \nu_\mu$) are given for all the models used in this paper as a function of $\Delta m^2/E_\nu$ and B at the surface of the neutronized iron core (B_0). Before we proceed to contour maps, the evolution of conversion probability in the isotopically neutral region along the trajectory of neutrinos is shown for some cases as a demonstration. Fig. 7 shows the conversion probability as a function of radius from the center of the star using the model NH4 for some values of B_0 , with $\Delta m^2/E_\nu = 10^{-4}$ [eV²/MeV], $\mu_\nu = 10^{-12} \mu_B$, and $\cos 2\theta = 1$. The resonance layer lies at $r \sim 5 \times 10^{-3} R_\odot$ in the O+Si layer and its location is never changed by strength of the magnetic fields. We can see in this figure that the conversion probability becomes larger with increasing strength of magnetic fields, and the complete conversion occurs with the magnetic fields strong enough ($B_0 \gtrsim 5 \times 10^9$ [Gauss], in this case) to satisfy the adiabaticity condition (see also Figure 3). Fig. 8 is the same with Fig. 7, but $\Delta m^2/E_\nu$ is 10^{-5} [eV²/MeV] and

the resonance layer is hence in more outer region at $r \sim 1.5 \times 10^{-2} R_{\odot}$ (O+Ne+Mg layer). As shown in these figures, the necessary B_0 for the complete conversion becomes larger with decreasing $\Delta m^2/E_{\nu}$ in the solar metallicity models, because the adiabaticity condition is well satisfied with larger $\Delta m^2/E_{\nu}$, as discussed in the previous section. In both the figures, the conversion probability jumps up a little at the radius of about $2.5 \times 10^{-3} R_{\odot}$, because this radius corresponds to the surface of the iron core and the value of $(1 - 2Y_e)$ drops quite suddenly here.

Now we calculate the contour maps of the conversion probability for the solar metallicity models, in the region of $\Delta m^2/E_{\nu} = 10^{-8}$ – 10^{-1} [eV²/MeV] and $B_0 = 10^8$ – 10^{10} [Gauss], and the results are given in Figs. 9–12 (for WW15S, WW25S, NH4, and NH8, respectively). In the region of $\Delta m^2/E_{\nu} < 10^{-8}$ [eV²/MeV] or $B_0 < 10^8$ [Gauss], the conversion does not occur because of too weak magnetic fields. Magnetic fields stronger than 10^{10} [Gauss] induce the precession below the surface of the iron core which cannot be ignored, and $\Delta m^2/E_{\nu}$ larger than 10^{-1} [eV²/MeV] leads to the resonance below the surface of the iron core. In this paper, we consider the parameter region in which the conversion or precession below the iron core surface can be neglected. The contours are depicted with the probability intervals of 0.1, assuming $\mu_{\nu} = 10^{-12} \mu_B$ and $\cos 2\theta = 1$. It can be seen that some observable effects on the spectrum of the emitted $\bar{\nu}_e$'s are expected if B_0 is stronger than $\sim 10^9$ [Gauss] and Δm^2 is larger than $\sim 10^{-5}$ [eV²]. Note that the typical energy range of the neutrinos which are observed in a water Čerenkov detector is 10–70 MeV. The lower margins of the strong conversion region ($P > 0.9$, where P is the conversion probability) in the contour maps are, in all the four models, contours which runs from the upper left to the lower right direction. This is due to the fact that the adiabaticity condition is well satisfied with larger values of $\Delta m^2/E_{\nu}$, as discussed in the previous section. We refer to this marginal region in the contour maps as “the continuous deformation region”, because the conversion probability continuously decreases with increasing neutrino energy in this region and the spectral deformation is expected to be continuous. What is interesting about these maps is that some band-like patterns can be seen in the relation of the conversion probability and the value of $\Delta m^2/E_{\nu}$. For example, the conversion probability in the region of $\Delta m^2/E_{\nu} = 5 \times 10^{-4}$ – 5×10^{-3} [eV²/MeV] in Fig. 11 is much lower than that in the other regions of the map. These patterns come directly from the jumps in the matter potential due to the onion-like structure of the isotopic composition in giant stars [11]. When $\Delta m^2/E_{\nu}$ is in the above region, the resonance in the model NH4 occurs at the surface of the iron core and the interval of $\Delta m^2/E_{\nu}$ corresponds to the jump of ΔV at the surface (see Fig. 3). Since the matter potential changes suddenly here, very strong magnetic field is necessary for the satisfaction of the adiabaticity condition, and consequently the resonant conversion is significantly suppressed. We refer to such bands of $\Delta m^2/E_{\nu}$ as “the weak adiabaticity band”, hereafter. At each boundaries of the onion-like structure of massive stars, this weak adiabaticity band appears due to the jump in the matter potential. It should also be noted that in the weak adiabaticity bands, the conversion probability only weakly depends on $\Delta m^2/E_{\nu}$ because the location of the resonance layer is not changed in a band. In Figs. 9–12, we can see the difference between the WW and NH models as well as between 15 and 25 M_{\odot} models. Although there are some quantitative differences, almost all qualitative features are the same for these four models.

Next we show the contour maps of the conversion probability for the zero metallicity models, in Figs. 13 and 14 (for the models WW15Z and WW25Z, respectively), with the region of $\Delta m^2/E_{\nu} = 10^{-11}$ – 10^{-1} [eV²/MeV] and $B_0 = 10^8$ – 10^{10} . When $\Delta m^2/E_{\nu}$ is larger than $\sim 10^{-6}$ [eV²/MeV],

the profile of the contour maps is qualitatively similar to that of the solar metallicity models. But the adiabaticity condition can be satisfied with smaller strength of magnetic fields and the region of complete conversion becomes somewhat larger, because in the inner part of the isotopically neutral region (O+Si and O+Ne+Mg layers) the value of $(1 - 2Y_e)$ is about 1 order of magnitude smaller than that in the solar metallicity models. Especially, in the model WW25Z, ΔH and $\mu_\nu B$ are comparable in this region (see Fig. 6) and the precession effect is no longer negligible, leading to the more complicated feature of the contour map of WW25Z than of WW15Z. When $\Delta m^2/E_\nu \lesssim 10^{-6}$ [eV²/MeV], the strong precession occurs in the outer part of the isotopically neutral region (O+C and He layers), where $\mu_\nu B$ is much higher than ΔH . In contrast to the solar metallicity models, the conversion still occurs with such a low value of $\Delta m^2/E_\nu$, even when $\Delta m^2 = 0$. Further interesting is that with $\Delta m^2/E_\nu$ lower than $\sim 10^{-6}$ [eV²/MeV], the conversion probability changes periodically with $\mu_\nu B_0$ (Fig. 13). This can be understood as follows. The precession effect in the outer part of the isotopically neutral region is very profound and then this precession is stopped almost suddenly at the boundary of the helium layer and the hydrogen envelope where $|\Delta V|$ increases by 5–10 orders of magnitude. The final phase of the precession strongly depends on $\mu_\nu B_0$, because the precession length is given as

$$L = \frac{\pi}{\sqrt{\left(\frac{\Delta m^2}{4E_\nu}\right)^2 + (\mu_\nu B)^2}}. \quad (12)$$

Therefore the conversion probability changes periodically with $\mu_\nu B_0$. The examples of strong precession effect are shown in Fig. 15, using the WW15Z model with $\Delta m^2 = 0$ and some values of B_0 . The conversion probability as a function of the radius is shown in this figure. The precession begins at $r = 0.025R_\odot$ and ceases at $r = 0.28R_\odot$ (see also Fig. 5). One can see that the precession length becomes larger with propagation of neutrinos, because B decreases with r . It is also clear that the change in B_0 leads to the change of the precession length, and hence to the oscillation of the final phase of precession. Below $\Delta m^2/E_\nu \sim 10^{-11}$ [eV²/MeV], the effect of the mass term can be completely neglected and the conversion probability becomes constant (but never vanishes) with neutrino mass or energy.

B. Spectral Deformation

All of the qualitative features of the spectral deformation due to the resonant spin-flavor conversion of $\bar{\nu}_e \leftrightarrow \nu_\mu$ are clearly understood by the contour maps given in the previous section (Figs. 9–14). The most easily detectable flavor in a water Čerenkov detector is $\bar{\nu}_e$'s because of the large cross section of the reaction $\bar{\nu}_e p \rightarrow n e^+$, and they are detectable above the positron energy of ~ 5 MeV in the Super-Kamiokande detector, which has the fiducial volume of 22,000 tons [1]. If we consider the positron energy range of 10–70 MeV, which includes almost all of the events, this range corresponds to a vertical bar in the contour maps with fixed values of Δm^2 and B_0 . The samples of such a bar are shown in Figs. 11 and 12 (NH models), and the corresponding spectral deformation of the events at the SK are shown in Fig. 16. The distance of the supernova is set to 10 kpc and the total energy of each type of neutrinos is assumed to be 5×10^{52} erg. We use 5 and 8 MeV as the temperature of $\bar{\nu}_e$'s and ν_μ 's, respectively, and the Fermi-Dirac distribution with

zero chemical potential is assumed for both $\bar{\nu}_e$'s and ν_μ 's [37]. The cross section of the dominant reaction of $\bar{\nu}_e p \rightarrow n e^+$ is $9.72 \times 10^{-44} E_e p_e \text{ cm}^2$ [1], where E_e and p_e is the energy and momentum of recoil positrons. The appropriate detection efficiency curve is also taken into account [38]. The thick solid line in Fig. 16 is the expected differential event number of $\bar{\nu}_e$'s without any oscillation or conversion.

As mentioned in the previous section, the three characteristic regions appear in the contour maps for the solar metallicity models: A) the complete conversion region, B) the continuous deformation region, and C) the weak adiabaticity band. (A, B, and C correspond to those in Figs. 11 and 12.) When the conversion is complete, we can see the original ν_μ spectrum as $\bar{\nu}_e$'s, and the event number is considerably enhanced because of the higher average energy (thin solid line in Fig. 16). When the vertical line in the contour map lies in the continuous deformation region, conversion probability decreases with increasing energy of neutrinos and consequently the original ν_μ 's are dominant in the lower energy range, while the original $\bar{\nu}_e$'s are dominant in the higher energy range (short-dashed line in Fig. 16, also corresponding to the vertical line (B) in Fig. 12). Note that this feature is based upon the assumption that the radial dependence of the magnetic fields is a dipole ($B \propto r^{-3}$) and $\mu_\nu B$ drops faster than $|d(\Delta V)/dr|^{1/2}$ with increasing radius. On the other hand, in the weak adiabaticity band, the energy dependence of conversion probability is rather weak (long-dashed line in Fig. 16, also corresponding to the vertical line (C) in Fig. 11). Because the resonance always occurs in the same place (jumps in the matter potential), this feature does not depend on the assumption of the radial dependence of magnetic fields, in contrast to the case (B). Finally, quite interesting deformation is expected if the vertical line in the contour maps crosses the boundary of the weak adiabaticity band (the vertical line (D) in Fig. 11). Because the conversion probability changes almost suddenly at the boundary, the spectrum of the event rate suffers drastical deformation at a certain positron energy (dot-dashed line in Fig. 16). The used values of (Δm^2 [eV²], B_0 [Gauss]) for the vertical lines A, B, C, and D in Figs. 11 and 12 are ($5 \times 10^{-3}, 7 \times 10^9$), ($5 \times 10^{-4}, 5 \times 10^9$), ($3 \times 10^{-2}, 5 \times 10^9$), and ($1.5 \times 10^{-2}, 2 \times 10^9$), respectively.

In the zero metallicity models, the feature of the spectrum deformation is similar to that of the solar metallicity models when $\Delta m^2/E_\nu \gtrsim 10^{-7}$ [eV²/MeV]. However, if $\Delta m^2 \sim 10^{-7}$ – 10^{-6} [eV²], the conversion probability increases with neutrino energy, because the precession in the outer part of the isotopically neutral region becomes effective (Fig. 13). With $\Delta m^2/E_\nu \lesssim 10^{-9}$ [eV²/MeV], the conversion probability becomes constant with neutrino energy, but changes periodically with B_0 . In the model WW25Z, the precession in the inner part of the isotopically neutral region (O+Si and O+Ne+Mg layers) is also effective, and the probability may change rapidly and complicatedly with neutrino energy (Fig 14).

V. DISCUSSION

We found that the difference of the stellar metallicity significantly affects the resonant spin-flavor conversion of $\bar{\nu}_e \leftrightarrow \nu_\mu$, and some implications from this fact are discussed in the following. The lifetime of massive stars which end their life by the gravitational collapses is very shorter than that of the Sun, and the progenitors of observed supernovae are therefore younger. Consequently, the metallicity of the Galactic supernova is expected to be at least the solar abundance or more metal-rich. If the metallicity is higher than that of the Sun, the suppression of $(1 - 2Y_e)$ will be

weaker and the B_0 which is required to satisfy the adiabaticity condition becomes larger. On the other hand, the Large and Small Magellanic Clouds are known to be very metal-poor systems [39]. Therefore, the resonant conversion will occur with smaller magnetic fields in supernovae in the Magellanic Clouds, and also the precession effect may be observed. The another object which has relation to the metallicity effect is the supernova relic neutrino background (SRN) [40]. Because the SRN is the accumulation of neutrinos from supernovae which have ever occurred in the universe, the SRN includes neutrinos from supernovae with quite low metallicity in the early phase of galaxy formation. The conversion of $\bar{\nu}_e \leftrightarrow \nu_\mu$ compensates the energy degradation due to the cosmological redshift effect and enhances the expected event rate of the SRN. However, because of the small expected event rate at the SK [40], it will be difficult to get some decisive information on the spin-flavor conversion from the observation at the SK.

We did not consider the flavor conversion (the MSW effect) in this paper although this can occur with appropriate generation mixing and neutrino masses. With the same $\Delta m^2/E_\nu$, the resonance of the flavor conversion occurs in more outer region than the resonance layer of the spin-flavor conversion, because the matter potential for the flavor conversion are not suppressed by $(1 - 2Y_e)$ [11]. Even if the flavor conversion occurs in more outer region, the spectrum of $\bar{\nu}_e$ is not changed. There may be interesting effect if we consider the conversion in the iron core, or the mutual effect of spin-flavor and flavor conversion among the three generations of neutrinos, as pointed out by the earlier publication [11].

The turbulence in the radial dependence of the magnetic fields was ignored in this paper. In the solar metallicity models, ΔH is much larger than $\mu_\nu B$ except at the resonance, and the conversion probability is determined only from the strength of the field at the resonance layer. Therefore the turbulence does not affect the evolution of conversion probability of neutrinos. However, the turbulence disturbs the relation of B_0 and B at the resonance layer. When the neutrino energy changes, the location of the resonance layer also changes, and hence the neutrino spectrum can be disturbed by some strong turbulence in the magnetic fields.

The effect of dynamics in the collapse-driven supernova was also not taken into consideration. Although it seems unlikely that the shock wave is propagated through the whole isotopically neutral region in a few tens of seconds, the inner part of the isotopically neutral region may be dynamically disturbed by the shock wave. If $\Delta m^2/E_\nu$ is large, the resonance occurs at the inner part of the isotopically neutral region, and the dynamical effect may change the situation of the resonant conversion of the neutrinos emitted in the later phase of emission ($\gtrsim 10$ sec after the bounce). We give here simple discussion on the effect of the change in density, assuming that Y_e is conserved during the shock propagation. (The composition of matter is drastically changed by the shock wave, but the change in Y_e requires the weak interaction.) The matter potential (ΔV) changes as $\propto \rho$. On the other hand, if we assume the conservation of the magnetic flux in dynamical plasma, the field strength changes as $\propto \rho^{2/3}$, and hence the precession becomes more effective with decreasing matter density (see Eq. (9)). However, the adiabaticity condition is the competition of $\mu_\nu B$ and $|d(\Delta V)/dr|^{1/2}$, and if we assume $|d(\Delta V)/dr|$ scales as (length) $^{-4}$ (homogeneous expansion or compression), the scaling of $|d(\Delta V)/dr|^{1/2}$ is the same with that of magnetic fields, $\propto \rho^{2/3}$. Therefore, the adiabaticity condition is not strongly affected by the dynamics of the shock wave.

It should also be noted that the observed data of neutrinos from SN1987A [28,29] favor a softer neutrino spectrum than theoretically plausible spectrum of electron antineutrinos. If $\bar{\nu}_e$'s are ex-

changed with ν_μ -like neutrinos (ν_μ, ν_τ , and their antiparticles) which have higher average energy, this discrepancy becomes larger. From this view point, an upper bound on the conversion probability of $\bar{\nu}_e$'s and ν_μ -like neutrinos has been derived: $P < 0.35$ at the 99 % confidence level [41]. The earlier paper of the spin-flavor conversion [11] used this constraint in order to derive an upper bound on the neutrino magnetic moment. However, the above constraint on P and its confidence level suffer considerable statistical uncertainty because of the small number of events in Kamiokande and IMB. Therefore, we avoid a decisive conclusion about the upper bound on μ_ν from SN1987A, although the strong conversion region ($P > 0.9$) in the contour maps (Figs. 9–14) may be disfavored. Also we point out here that the metallicity effect on the conversion probability should be taken into account when one attempts to constrain μ_ν from the SN1987A data, because the Large Magellanic Cloud is a low-metal system.

VI. CONCLUSIONS

Neutrino spin-flavor conversion of $\bar{\nu}_e \leftrightarrow \nu_\mu$ induced by the interaction of a flavor changing magnetic moment of Majorana neutrinos and magnetic fields above the iron core of collapsing stars was investigated in detail. The effective matter potential of this conversion mode ($\bar{\nu}_e \leftrightarrow \nu_\mu$) is proportional to $(1 - 2Y_e)$, and hence this value is quite important to this resonant conversion. However, this value is determined by isotopes which are quite rarely existent, and in order to estimate the effect of the astrophysical uncertainties, we used the six precollapse models, changing the stellar masses, metallicities, and authors of the models. The components of Hamiltonian in the propagation equation (5) are shown for all the models in Figs. 1–6, and qualitative features of the conversion can be understood from these figures. The results of the numerical calculation for all the models are shown in Figs. 9–14 as contour maps of conversion probability as a function of the two parameters of $\Delta m^2/E_\nu$ and B_0 , where B_0 is B at the surface of the iron core.

For the solar metallicity models, observable effects are expected when $\Delta m^2/E_\nu$ is in the range of 10^{-5} – 10^{-1} [eV²/MeV] and $\mu_\nu \gtrsim 10^{-12}(10^9\text{G}/B_0)$ [μ_B] (Figs. 9–12). The difference of the stellar masses leads to the different thickness and location of the layers of the onion-like structure in massive stars and this effect appears in the contour maps, although the effect is rather small. The qualitative features of the contour maps for the WW and NH models are also not so different, and the model dependence of the conversion probability can be roughly estimated by the comparison of these figures. Although the dependence on the stellar models or stellar masses is rather weak as shown in Figs. 9–12, it was found that the metal abundance of the precollapse star significantly affect the value of $(1 - 2Y_e)$. The difference between the solar and zero metallicity is prominent especially in the O+C and He layers, and the strong precession between $\bar{\nu}_e \leftrightarrow \nu_\mu$ occurs with small $\Delta m^2/E_\nu$, because $\mu_\nu B$ is much larger than $\Delta m^2/E_\nu$ in this region. In contrast to the solar metallicity models, the conversion occurs even when $\Delta m^2 = 0$. The probability changes periodically with B_0 because of the precession effect. (See Figs. 13 and 14.)

Considering the above properties, the expected spectral deformation of $\bar{\nu}_e$'s can be summarized as follows. For the solar metallicity models, there are roughly three types of the energy dependence of the conversion probability: 1) complete conversion in a range of neutrino energy, 2) conversion probability decreases with increasing energy when the energy range is in ‘the continuous deformation region’ in the contour maps, and 3) incomplete conversion and weak energy dependence

of conversion probability when the energy range is in ‘the weak adiabaticity band’ in the contour maps. Examples of these types of spectral deformation are given in Fig. 16. (For the explanation of ‘the continuous deformation region’ and ‘the weak adiabaticity band’, see section IV.) Furthermore, there appear some interesting jumps in the spectrum if the energy range of 10–70 MeV includes boundaries of the complete conversion region and the weak adiabaticity band. Irrespective of the stellar models or stellar masses, such a boundary exists especially at the surface of the iron core, where the matter potential suddenly changes. For the zero metallicity models, although the feature of the spectral deformation is similar to that of the solar metallicity models when $\Delta m^2/E_\nu \gtrsim 10^{-7}$ [eV²/MeV], energy-independent conversion is possible with quite small $\Delta m^2/E_\nu$ ($\lesssim 10^{-9}$ [eV²/MeV]), which does not occur in the solar metallicity models.

ACKNOWLEDGMENTS

The authors would like to thank S.E. Woosley and M. Hashimoto, for providing us the data of their precollapse models and useful comments. They are also grateful to Y. Totsuka, for the information on the detection efficiency of the SK detector. This work has been supported in part by the Grant-in-Aid for COE Research (07CE2002) and for Scientific Research Fund (05243103 and 07640386) of the Ministry of Education, Science, and Culture in Japan.

-
- [1] Y. Totsuka, Rep. Prog. Phys. **55**, 377 (1992); K. Nakamura, T. Kajita, M. Nakahata, and A. Suzuki, *Kamiokande, in Physics and Astrophysics of Neutrinos*, edited by M. Fukugita and A. Suzuki (Springer-Verlag, Tokyo, 1994).
 - [2] L. Wolfenstein, Phys. Rev. D **17**, 2369 (1978); S. P. Mikheyev and A. Yu. Smirnov, Yad. Fiz. **42**, 1441 (1985) [Sov. J. Nucl. Phys. **42**, 913 (1985)]; Nuovo Cim. **9C**, 17 (1986).
 - [3] A. Cisneros, Astrophys. Space Sci. **10**, 87 (1970)
 - [4] K. Fujikawa and R. E. Shrock, Phys. Rev. Lett. **45**, 963 (1980).
 - [5] J. Schechter and J. W. F. Valle, Phys. Rev. D **24**, 1883 (1981); **25**, 283 (E) (1982).
 - [6] C. S. Lim and W. J. Marciano, Phys. Rev. D **37**, 1368 (1988).
 - [7] E. Kh. Akhmedov, Sov. J. Nucl. Phys. **48**, 382 (1988); Phys. Lett. B **213**, 64 (1988).
 - [8] M. B. Voloshin, Phys. Lett. B **209**, 360 (1988).
 - [9] E. Kh. Akhmedov and Z. G. Berezhiani, Nucl. Phys. B **373**, 479 (1992).
 - [10] J. T. Peltoniemi, Astron. Astrophys. **254**, 121 (1992).
 - [11] H. Athar, J. T. Peltoniemi, and A. Yu. Smirnov, Phys. Rev. D **51**, 6647 (1995).

- [12] M. Fukugita and S. Yazaki, Phys. Rev. D **36**, 3817 (1987).
- [13] G. G. Raffelt, Phys. Rev. Lett. **64**, 2856 (1990); Astrophys. J. **365**, 559 (1990).
- [14] W. J. Marciano and A. I. Sanda, Phys. Lett. B **67**, 303 (1977).
- [15] B. W. Lee and R. E. Shrock, Phys. Rev. D **16**, 1444 (1977).
- [16] S. T. Petkov, Yad. Fiz. **25**, 641 (1977) [Sov. J. Nucl. Phys. **25**, 340 (1977)].
- [17] M. Fukugita and T. Yanagida, Phys. Rev. Lett. **58**, 1807 (1987).
- [18] K. S. Babu and V. S. Mathur, Phys. Lett. B **196**, 218 (1987).
- [19] M. B. Voloshin, M. I. Vysotskiĭ, and L. B. Okun, Yad. Fiz. **44**, 677 (1986) [Sov. J. Nucl. Phys. **44**, 440 (1986)]; Zh. Eksp. Teor. Fiz. **91**, 754 (1986) [Sov. Phys. JETP **64**, 446 (1986)].
- [20] E. Kh. Akhmedov, Zh. Eksp. Teor. Fiz. **95**, 1195 (1989) [Sov. Phys. JETP **68**, 690 (1989)].
- [21] K. Inoue, Ph. D. thesis, The University of Tokyo, 1993.
- [22] G. A. Bazilevskaya, Yu. I. Stozhkov, and T. N. Charakhchyan, Pis'ma Zh. Eksp. Teor. Fiz. **35**, 273 (1982) [JETP Lett. **35**, 341 (1982)]; G. A. Bazilevskaya et al., Yad. Fiz. **39**, 856 (1984) [Sov. J. Nucl. Phys. **39**, 543 (1984)]; R. Davis, Jr., in *Solar Neutrinos and Neutrino Astronomy—1984*, AIP Conference Proceedings No. 126, edited by M. L. Cherry, K. Lande, and W. A. Fowler (American Institute of Physics, New York, 1985).
- [23] Y. Raphaeli and A. S. Szalay, Phys. Lett. B **106**, 73 (1981).
- [24] S. Nusseinov and Y. Raphaeli, Phys. Rev. D **36**, 2278 (1987).
- [25] S. E. Woosley and T. A. Weaver, Astrophys. J. Suppl. **101**, 181 (1995).
- [26] K. Nomoto and M. Hashimoto, Phys. Rep. **163**, 13 (1988).
- [27] E. Kh. Akhmedov et al., preprint SISSA 40/96/A-EP (hep-ph/9603443) (1996).
- [28] K. S. Hirata et al., Phys. Rev. Lett. **58**, 1490 (1987); Phys. Rev. D **38**, 448 (1988).
- [29] R. M. Bionta et al., Phys. Rev. Lett. **58**, 1494 (1987); C. B. Bratton et al., Phys. Rev. D **37**, 3361 (1988).
- [30] A. Dar, SLAC preprint (1987), unpublished.
- [31] J. M. Lattimer and J. Cooperstein, Phys. Rev. Lett. **61**, 23 (1988).
- [32] R. Barbieri and R. N. Mohapatra, Phys. Rev. Lett. **61**, 27 (1988).
- [33] D. Nötzold, Phys. Rev. D **38**, 1658 (1988).
- [34] S. E. Woosley and T. A. Weaver, Annu. Rev. Astron. Astrophys. **24**, 205 (1986).
- [35] S. E. Woosley, N. Langer, and T. A. Weaver, Astrophys. J. **411**, 823 (1993).

- [36] G. Chanmugam, *Annu. Rev. Astron. Astrophys.* **30**, 143 (1992).
- [37] For the properties of supernova neutrinos, see, e.g., A. Burrows, D. Klein, and R. Gandhi, *Phys. Rev. D* **45**, 3361 (1992), and references therein.
- [38] Y. Totsuka, private communication (1994).
- [39] For recent observations, see, e.g., M. Hilker, T. Richtler, and W. Gieren, *Astron. Astrophys.* **294**, 648 (1995); M.T. Meliani, B. Barbuy, and T. Richtler, *Astron. Astrophys.* **304**, 347 (1995).
- [40] T. Totani and K. Sato, *Astropart. Phys.* **3**, 367 (1995); T. Totani, K. Sato, and Y. Yoshii, *Astrophys. J.* **460**, 303 (1996), and references therein.
- [41] A. Yu. Smirnov, D. N. Spergel, and J. N. Bahcall, *Phys. Rev. D* **49**, 1389 (1994).

TABLES

TABLE I. The table of $(1 - 2Y_e)$ in the isotopically neutral region (O+Si, O+Ne+Mg, O+C, and He layers) for all the models of precollapse stars used in this paper. The models WW15 and WW25 are 15 and 25 M_\odot models by Woosley and Weaver (1995) [25]. There are models with two different metallicities in the WW models, and they are distinguished by ‘S’ (solar metallicity) and ‘Z’ (zero metallicity). The models NH4 and NH8 are 4 and 8 M_\odot helium core models (corresponding approximately to 15 and 25 M_\odot main sequence stellar masses) by Nomoto and Hashimoto (1988) [26]. The isotopes in the parentheses under the values of $(1 - 2Y_e)$ are the main isotopes which cause the deviation of Y_e from 0.5.

Model	O+Si	O+Ne+Mg	O+C	He
WW15S	2×10^{-3} (³⁴ S, ³⁸ Ar)	2×10^{-3} (²³ Na, ^{25,26} Mg)	2×10^{-3} (²² Ne, ²⁵ Mg)	$1-10 \times 10^{-4}$ (¹⁸ O, ⁵⁶ Fe)
WW25S	2×10^{-3} (³⁴ S, ³⁸ Ar)	2×10^{-3} (^{25,26} Mg, ²⁷ Al)	2×10^{-3} (²² Ne, ^{25,26} Mg)	2×10^{-3} (²² Ne)
WW15Z	$6-10 \times 10^{-4}$ (²⁷ Al, ^{29,30} Si)	4×10^{-4} (²³ Na, ²⁶ Mg)	$1-6 \times 10^{-8}$ (²² Ne, ²⁶ Mg)	$2-100 \times 10^{-10}$ (¹⁸ O)
WW25Z	4×10^{-4} (²⁷ Al, ³⁰ Si)	1×10^{-4} (²³ Na, ²⁶ Mg)	2×10^{-7} (²² Ne, ^{25,26} Mg)	2×10^{-7} (^{13,14} C, ²² Ne)
NH4	1×10^{-3} (³⁴ S, ³⁸ Ar)	2×10^{-3} (^{25,26} Mg, ²⁷ Al)	2×10^{-3} (²² Ne, ²⁶ Mg)	2×10^{-3} (¹⁸ O, ²² Ne)
NH8	2×10^{-3} (²⁷ Al, ^{29,30} Si)	1×10^{-3} (²³ Na, ^{25,26} Mg)	1×10^{-3} (²² Ne, ²⁶ Mg)	2×10^{-3} (¹⁸ O, ²² Ne)

Figure Captions

FIG. 1. The components of the Hamiltonian in the propagation equation (5) are shown for the Woosley & Weaver’s solar-metallicity $15 M_{\odot}$ model, as a function of the radius from the center of the star. The absolute value of the effective matter potential, ΔV , is shown by the thick, solid line. The absolute value of the difference of the diagonal components of the Hamiltonian, ΔH , is shown by the dashed lines for the two values of the mass term, $\Delta m^2/E_{\nu} = 10^{-4}$ and 10^{-6} [eV²/MeV]. The resonant conversion occurs where $\Delta H = 0$ (the resonance layer). The dotted lines show $\mu_{\nu}B$, i.e., the off-diagonal components of the Hamiltonian. The indicated values of B are those at the surface of the iron core (B_0) in units of Gauss, assuming $\mu_{\nu} = 10^{-12} \mu_B$. The thin solid line shows $|d(\Delta V)/dr|^{1/2}$ [eV], and the adiabaticity condition is satisfied when $\mu_{\nu}B \gtrsim |d(\Delta V)/dr|^{1/2}$ at the resonance layer. The dot-dashed line shows $\mu_{\nu}B_{th}$, again assuming $\mu_{\nu} = 10^{-12} \mu_B$, where B_{th} is the magnetic field whose energy density is the same with the thermal energy density in the star. The dominantly existent nuclei in each layer of the precollapse model are shown in the top of this figure.

FIG. 2. The same as Fig. 1, but for the Woosley & Weaver’s solar-metallicity $25 M_{\odot}$ model.

FIG. 3. The same as Fig. 1, but for the Nomoto & Hashimoto’s $4 M_{\odot}$ helium-core model.

FIG. 4. The same as Fig. 1, but for the Nomoto & Hashimoto’s $8 M_{\odot}$ helium-core model. The O+Si and O+C layers are negligibly thin in this figure.

FIG. 5. The same as Fig. 1, but for the Woosley & Weaver’s zero-metallicity $15 M_{\odot}$ model. Note that the scale of the vertical axis is different from the previous four figures.

FIG. 6. The same as Fig. 1, but for the Woosley & Weaver’s zero-metallicity $25 M_{\odot}$ model.

FIG. 7. The evolution of conversion probability with the radius from the center of the star. The Nomoto & Hashimoto’s $4 M_{\odot}$ helium-core model is used, and $\Delta m^2/E_{\nu}$ is assumed to be 10^{-4} [eV²/MeV]. The four different values of B_0 are used for the calculation, where B_0 is the magnetic field at the surface of the iron core. The neutrino magnetic moment, μ_{ν} , is assumed to be $10^{-12} \mu_B$.

FIG. 8. The same as Fig. 7, but for the case with $\Delta m^2/E_{\nu} = 10^{-5}$ [eV²/MeV]. The three values of B_0 are used as indicated in the figure.

FIG. 9. The contour map of conversion probability for the Woosley & Weaver’s solar-metallicity $15 M_{\odot}$ model, as a function of $\Delta m^2/E_{\nu}$ and B_0 , where B_0 is the magnetic field at the surface of the iron core. The neutrino magnetic moment, μ_{ν} , is assumed to be $10^{-12} \mu_B$. The contours are depicted with the interval of 0.1.

FIG. 10. The same as Fig. 9, but for the Woosley & Weaver’s solar-metallicity $25 M_{\odot}$ model.

FIG. 11. The same as Fig. 9, but for the Nomoto & Hashimoto’s $4 M_{\odot}$ helium-core model. The two vertical bars, (C) and (D) correspond to the energy range of 10–70 MeV with $(\Delta m^2 [\text{eV}^2], B_0[\text{Gauss}]) = (3 \times 10^{-2}, 5 \times 10^9)$ and $(1.5 \times 10^{-2}, 2 \times 10^9)$, respectively, where the energy range is that of positrons which are observed in a water Čerenkov detector.

FIG. 12. The same as Fig. 11, but for the Nomoto & Hashimoto’s $8 M_{\odot}$ helium-core model. The values of $(\Delta m^2 [\text{eV}^2], B_0 [\text{Gauss}])$ for the two vertical bars, (A) and (B) are $(5 \times 10^{-3}, 7 \times 10^9)$ and $(5 \times 10^{-4}, 5 \times 10^9)$, respectively.

FIG. 13. The same as Fig. 9, but for the Woosley & Weaver’s zero-metallicity $15 M_{\odot}$ model. Note that the region of $\Delta m^2/E_{\nu}$ is different from that in Figs. 9–12.

FIG. 14. The same as Figure 13, but for the Woosley & Weaver’s zero-metallicity $25 M_{\odot}$ model.

FIG. 15. The same as Fig. 7, but for the Woosley & Weaver’s zero-metallicity $15 M_{\odot}$ model and $\Delta m^2/E_{\nu} = 0$. The three values of B_0 are used as indicated in the figure. Strong precession occurs in the region of $0.025\text{--}0.28 R_{\odot}$.

FIG. 16. Examples of the spectral deformation of $\bar{\nu}_e$ ’s for the solar metallicity models. The expected time-integrated differential events at the SK detector are shown, assuming that the supernova occurs in the Galactic center ($D = 10$ kpc). The upper box shows the corresponding conversion probability of $\bar{\nu}_e \leftrightarrow \nu_{\mu}$. The thick solid line shows the ordinary expected events of $\bar{\nu}_e$ ’s without any oscillation or conversion, and the thin solid line the differential events when all of the original ν_{μ} ’s are completely converted to $\bar{\nu}_e$ ’s in the whole energy range. The short dashed line is the events when $(\Delta m^2[\text{eV}^2], B_0[\text{Gauss}]) = (5 \times 10^{-4}, 5 \times 10^9)$, using the model NH8, corresponding to the case (B) in Fig. 12. The long-dashed and dot-dashed lines are differential events with $(\Delta m^2, B_0) = (3 \times 10^{-2}, 5 \times 10^9)$ and $(1.5 \times 10^{-2}, 2 \times 10^9)$, respectively, and the model NH4 is used for both the lines. The former corresponds to the bar (C) and the latter to the bar (D) in Fig. 11.

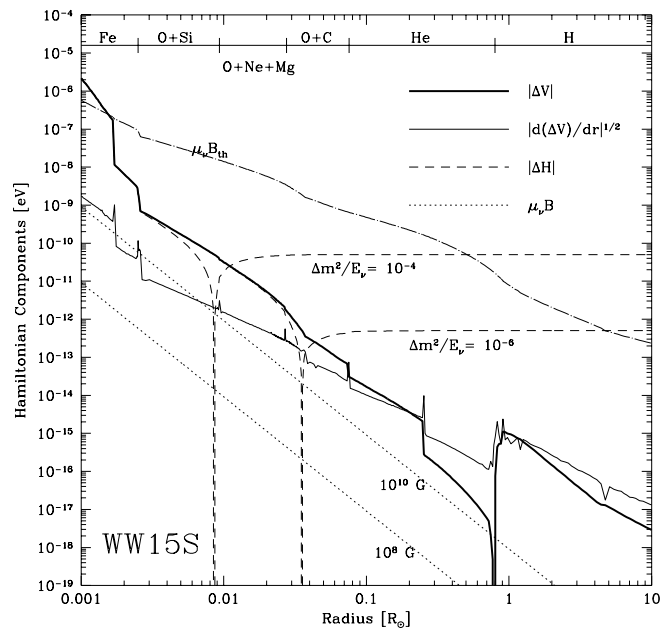


Fig. 1

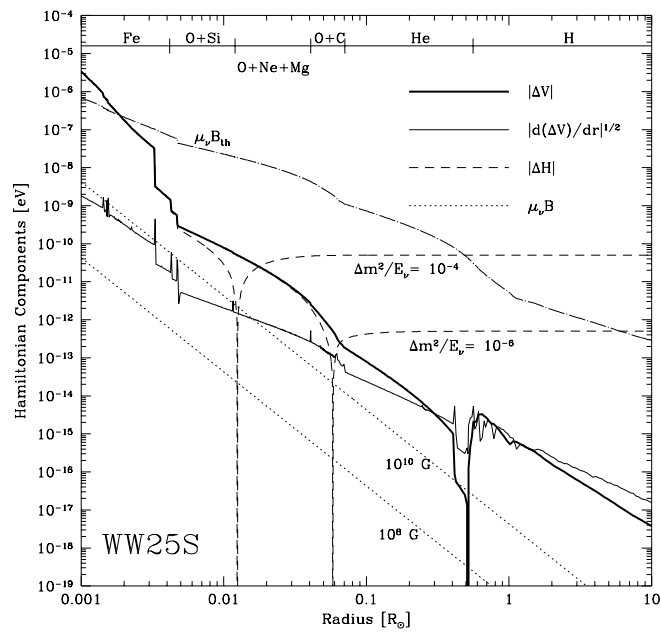


Fig. 2

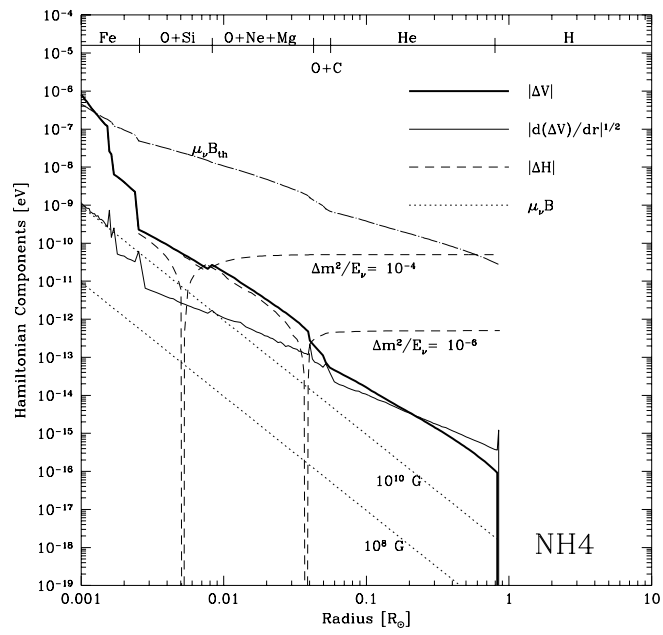


Fig. 3

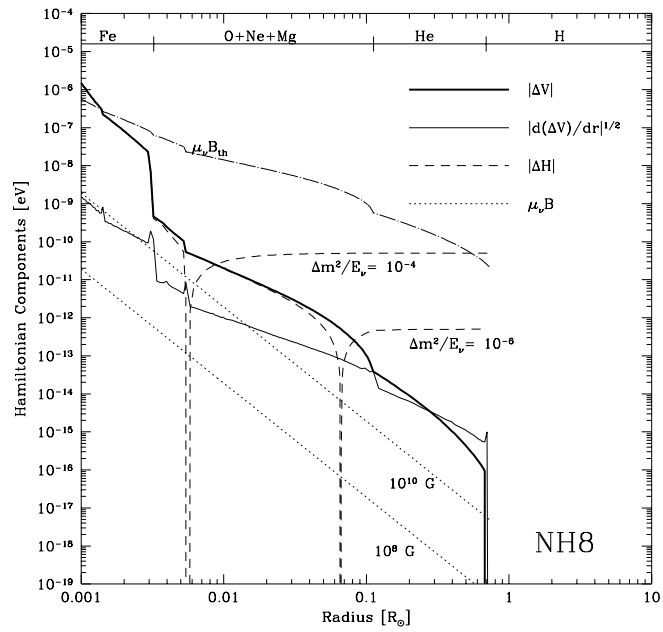


Fig. 4

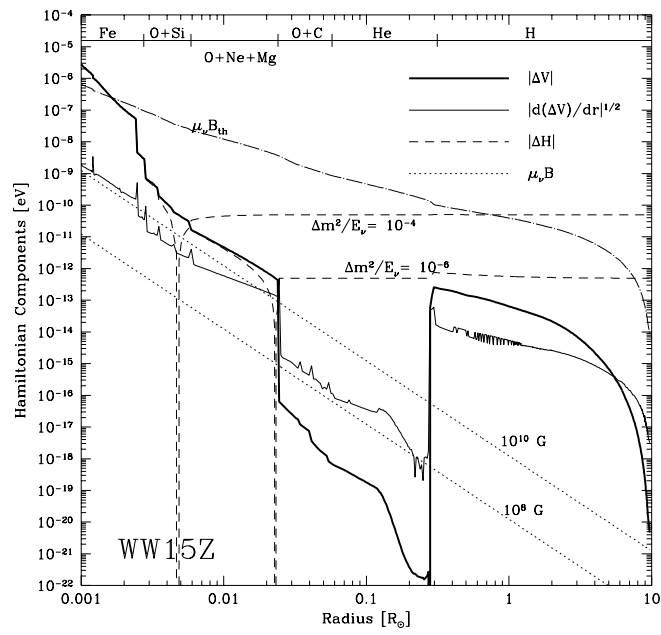


Fig. 5

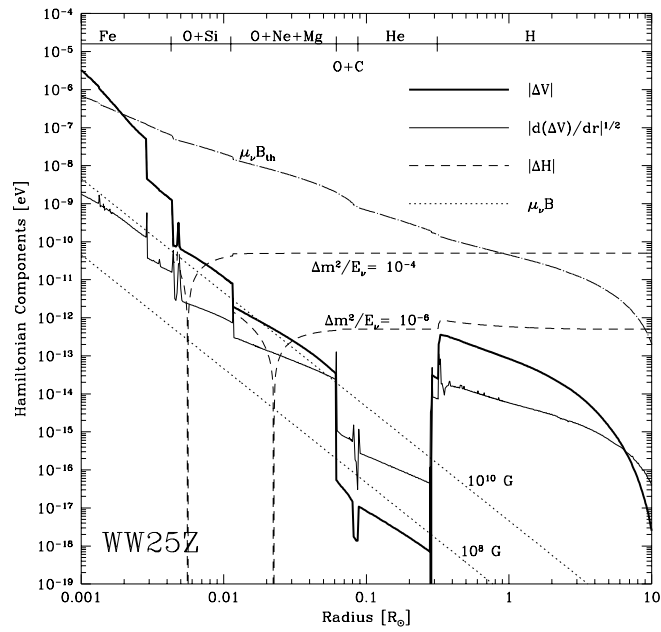


Fig. 6

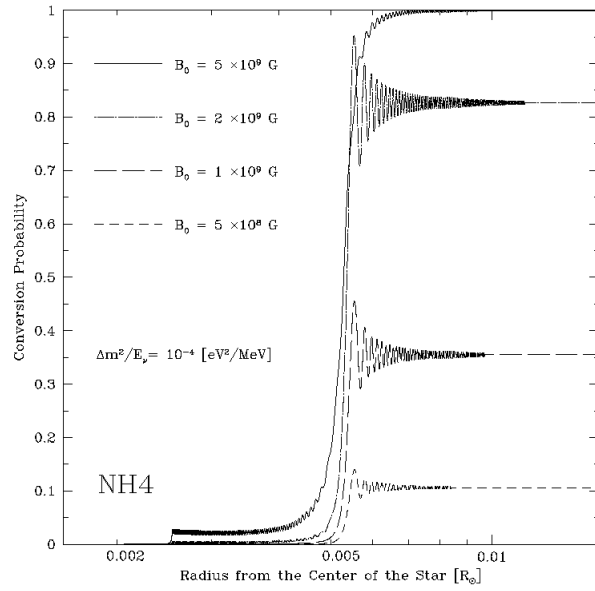


Fig. 7

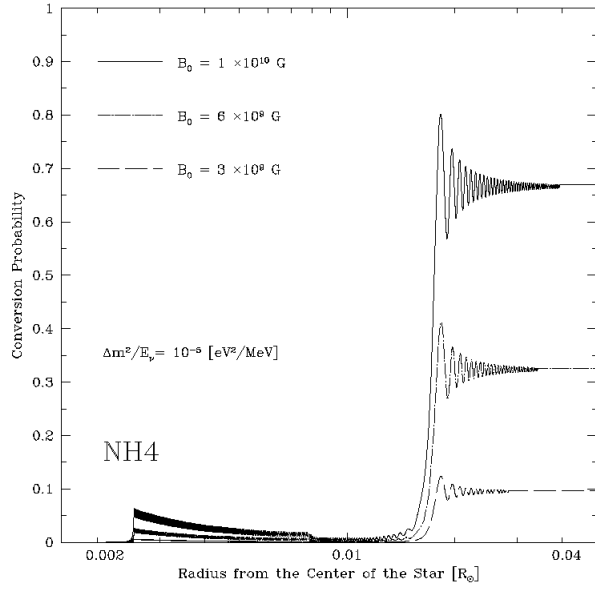


Fig. 8

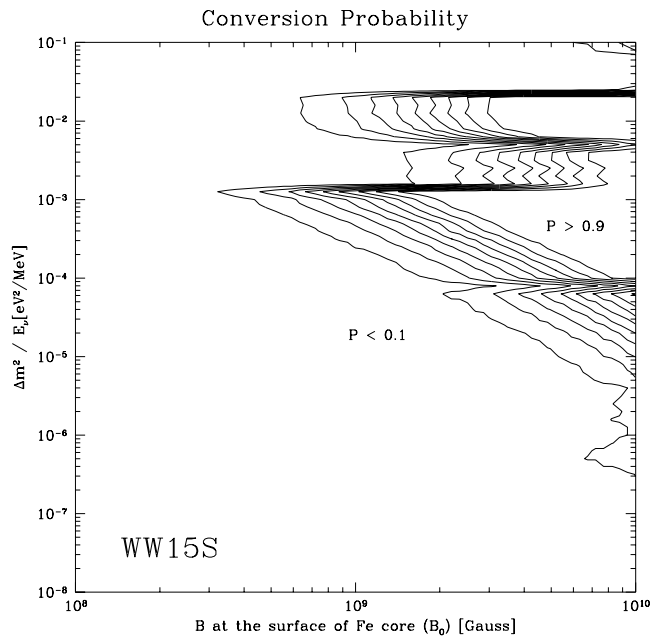


Fig. 9

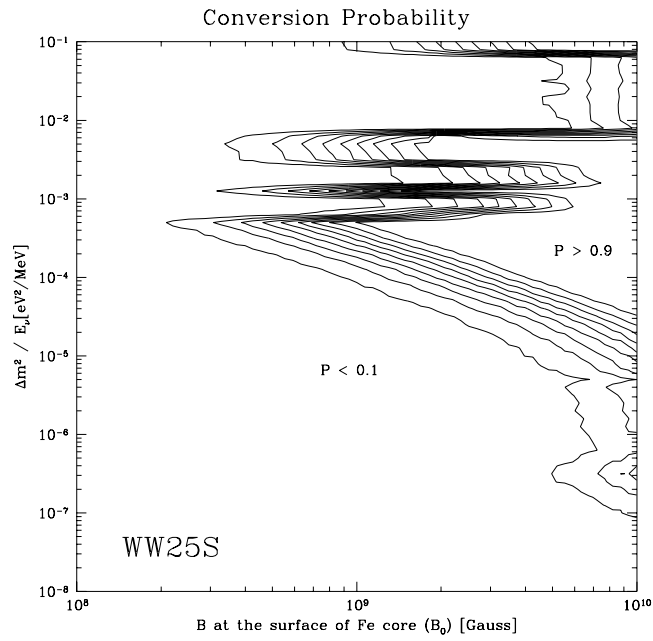


Fig. 10

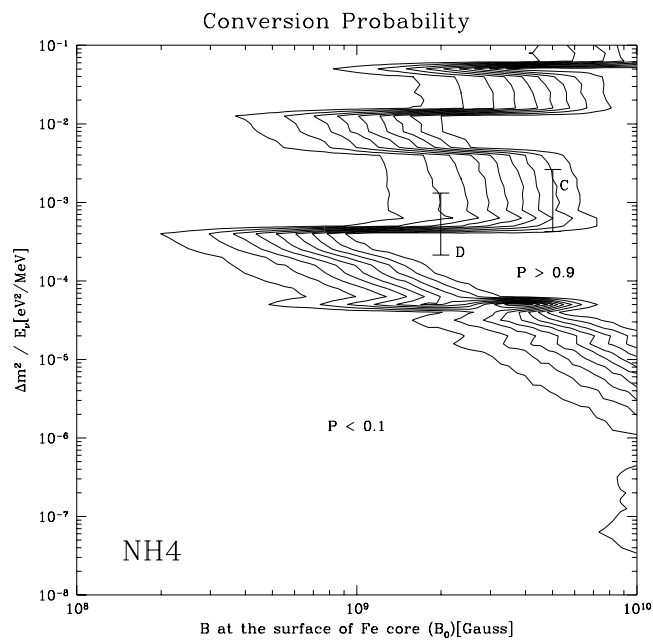


Fig. 11

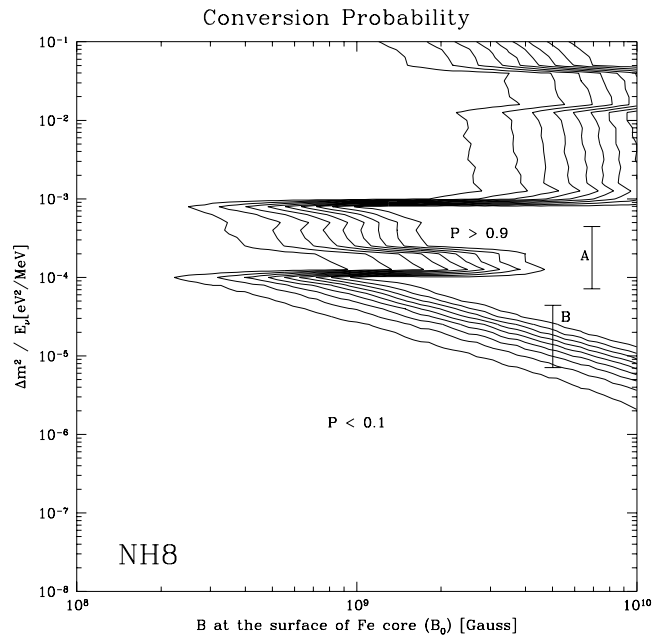


Fig. 12

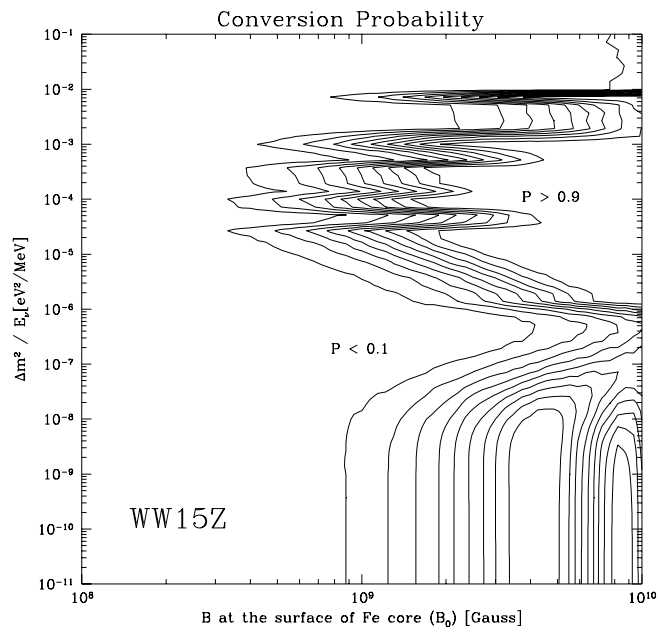


Fig. 13

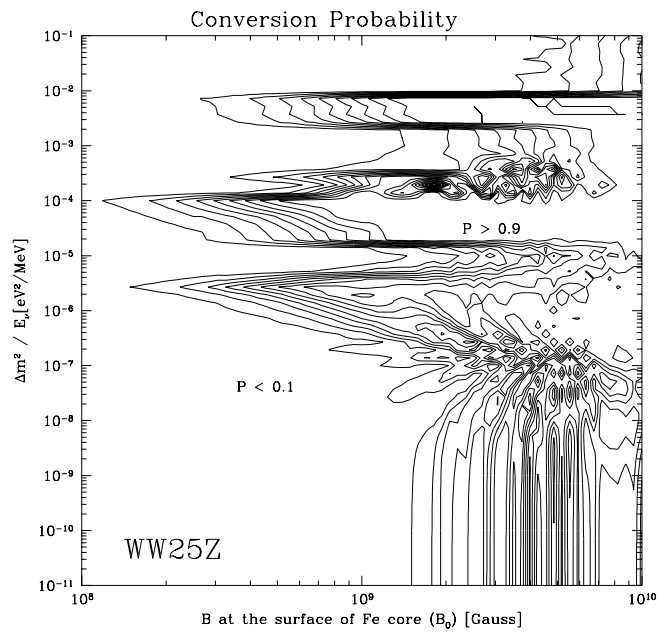


Fig. 14

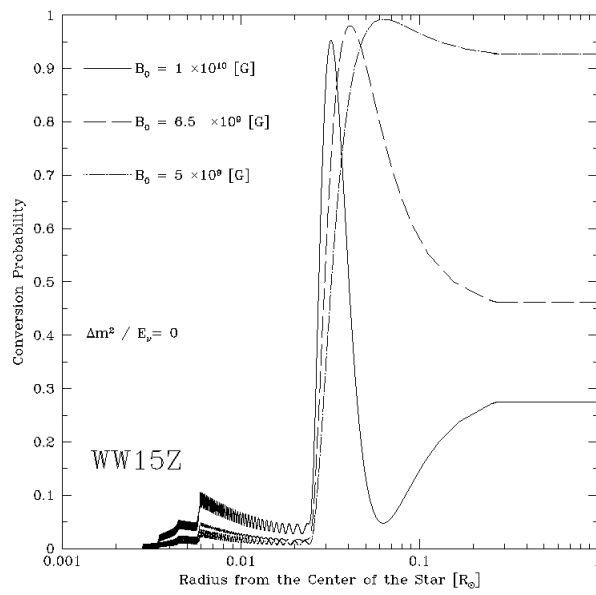


Fig. 15

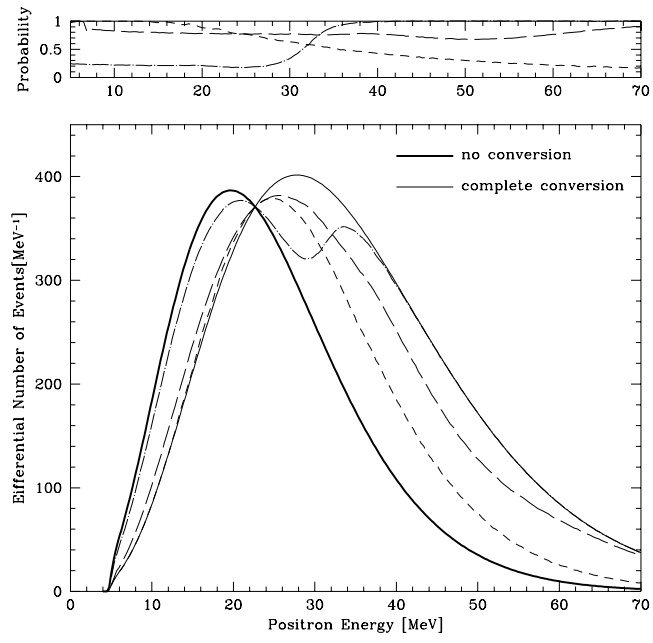


Fig. 16